Model-based optimization for combined interdigitated and serpentine flow field in redox flow batteries

Yansong Luo, Menglian Zheng, Jie Sun & Baichen Liu

View supplementary material 🗗

Published online: 06 Apr 2022.

Submit your article to this journal 🗗

Article views: 150

View related articles 🗗

View Crossmark data 🗗

Taylor & Francis
Taylor & Francis Group

Check for updates

Model-based optimization for combined interdigitated and serpentine flow field in redox flow batteries

Yansong Luo[a], Menglian Zheng[a,b], Jie Sun[a], and Baichen Liu[a]

[a]School of Energy Engineering, Institute of Thermal Science and Power Systems, Zhejiang University, Hangzhou, China; [b]State Key Laboratory of Clean Energy Utilization, School of Energy Engineering, Zhejiang University, Hangzhou, China

ABSTRACT

Interdigitated flow field and serpentine flow field are widely adopted in redox flow batteries, but their superiority cannot be determined independently of the operating conditions, electrode properties, and electrolyte properties. Matching the flow field to the operating conditions can effectively improve the efficiency of flow cells. To this end, the present study proposes a model-based optimization method to promote the system energy efficiency of flow cells by combining the interdigitated and serpentine flow channels and considering the heterogeneous distribution of reactants. The fluid dynamic model, electrochemical model, and genetic algorithm are integrated into an optimization framework in the present study to obtain the novel interdigitated-serpentine flow field. Simulative results show that compared to the interdigitated or serpentine flow field, the optimized interdigitated-serpentine flow field yields increments in the system energy efficiency ranging from 2% to 20% under varying operation conditions.

1. Introduction

Redox flow batteries (RFBs) are widely regarded as one of the most promising energy storage technologies for relieving the temporal discrepancies between power demand and supply, thereby enhancing the reliability of future energy systems integrated with a portfolio of fluctuating renewables (Weber et al. 2011). RFBs typically possess multiple advantages such as independent modular design, good scalability, and low levelized cost of storage (Pan and Wang 2015; Skyllas-Kazacos et al. 2011; Wang et al. 2013; Weber et al. 2011). However, the relatively high capital cost for a RFB system remains a critical barrier to the wide commercialization of RFBs (Noack et al. 2016). Although a dramatic reduction in the RFB capital cost is expected in the near term as a great amount of effort has been devoted to the development of novel metal-free electrolytes, which can be massively produced at low expenses (e.g., Huskinson et al. 2014; Zhang, Li, and Chu 2016), RFBs may suffer from low system efficiencies in real-world applications due to the limited mass transfer capability and the high pump power consumption during charge and discharge cycles (Shigematsu 2019). Furthermore, an enhancement in the mass transfer of reactants promotes the peak power density that can be applied to RFBs, which in turn reduces the total cost of the battery system at the given charge and discharge power (Houser et al. 2017; Xu, Zhao, and Zhang 2014).

For delivering reactants to the porous electrodes uniformly at the low expense of the pump power, a variety of flow fields have been devised and investigated extensively in previous studies. Apart from some niche flow field designs such as spiral (Huang et al. 2021), bio-inspired (Guo, Leu, and Koylu 2014),

trapezoid (Yue et al. 2018) 3-D detached (Sun et al. 2019), and obstructed flow fields (Akuzum et al. 2019), interdigitated flow field (IFF) and serpentine flow field (SFF) are two widely adopted flow fields with distinct characteristics. Specifically, the IFF is devised such that the volumetric electrolyte flow is forced through the porous electrode completely as a consequence of physical impediments (Gundlapalli and Jayanti 2020b). Based on such a mechanism, the analytical expression for the intra-electrode velocity and the pressure drop in the flow cell with the IFF was put forward by the previous studies (Darling and Badrinarayanan 2011; Darling and Perry 2014). Unlike the IFF, the SFF typically consists of physically connected flow passages, leading to the intra-electrode flow as a result of the balance between the hydraulic resistances of the flow channels and the electrode (Ke et al. 2018). This feature of the SFF makes the analytical expression of the intra-electrode flow under the SFF complicated. Ke et al. conducted a series of studies on the underlying mechanisms for the intra-electrode flow under the SFF and concluded that the intra-electrode flow was largely driven by the pressure gradient between two adjacent channels (Ke et al. 2014, 2015, 2018). Their simulative results showed that the volumetric electrolyte flow rate penetrating into the electrode beneath the flow passages is approximately 100 times that beneath the corner channels connecting parallel flow passages (Ke et al. 2018). The flow rate penetrating into the electrode beneath the flow passages was analytically investigated according to Darcy's law by Park and Li (2011), which was further corrected and validated with an inertial effect by Zhang et al. (2018). Based on the previous studies on the drivers for the intra-electrode flow, though the

CONTACT Menglian Zheng ✉ menglian_zheng@zju.edu.cn 🏢 Institute of Thermal Science and Power Systems, School of Energy Engineering, Zhejiang University, Hangzhou, 310027, China
⬆ Supplemental data for this article can be accessed on the publisher's website.

performance of RFBs with the IFF or the SFF were both closely associated with the permeability (Ke et al. 2018) and the thickness of the porous electrode (Kumar and Jayanti 2017), the Reynolds number of the electrolyte flow (Gundlapalli and Jayanti 2020b), and the geometric parameters of the flow field (Gundlapalli and Jayanti 2019, 2020a; Lee, Kim, and Park 2019), these parameters show distinct effects on the performance of the cell with the IFF and the SFF.

Recognizing the distinct characteristics of the SFF and the IFF with respect to the mechanisms for the intra-electrode electrolyte flow, it is understandable that the competing superiority results between the SFF and the IFF have been observed in a number of previous studies. For example, Kumar et al. reported the cell with the SFF showed a higher energy efficiency and a lower pressure drop compared to that under the IFF (Kumar and Jayanti 2016). However, the results obtained by Maurya et al. found that the IFF led to better performance than the SFF (Maurya et al. 2018). Similarly, Latha et al. compared the hydrodynamic results of the flow cells with the IFF and the SFF, respectively, and found that the pressure drop in the cell with the IFF was less than that with the SFF under the same flow rate (Latha and Jayanti 2014). The opposite results in different studies can be confusing, yet Houser et al. draw a conclusion that the superiority between the IFF and the SFF was largely dependent on the operating conditions, electrode properties (particularly geometry and permeability), and electrolyte properties (Houser et al. 2016).

Although a number of previous studies have investigated and improved the IFF and the SFF designs to extend the limiting current density and the peak power density of an RFB cell, few of them have considered the combination of the interdigitated and the serpentine flow channels to make the most of the associated benefits to these two distinct structures. Su et al. proposed a serpentine-interdigitated flow field and confirmed its better water removal efficiency in a small flow cell (Su et al. 2006). However, it remains unclear how to combine these two flow fields under various operating conditions. Furthermore, a concentration polarization due to the reactant concentration gradient especially at high state of charge and high current densities was reported by Zheng et al. (2016), which indicates that the flow battery should be heterogeneous to pursue the concert between the reactant concentration distribution and the intra-electrode velocity distribution. To meet the heterogeneous mass transfer requirements, some heterogeneous electrode architectures have been proposed in the through-plane or the in-plane directions of the electrode. For example, Yoon et al. proposed to adjust the porosity of the electrode to a lower value near the inlet of the flow cell compared to that near the outlet, for meeting the locally high mass transfer requirement near the inlet (Yoon, Kim, and Kim 2019). Identically, Gurieff et al. proposed a variable electrode compression for making the delivery of the reactants in concert with the consumption of the reactants in the through-plane direction (Gurieff, Timchenko, and Menictas 2018). However, similar consideration has not been taken into account in the design of the flow field, which plays a critical role in meeting the electrolyte mass transfer requirements.

Recently, the fast development of the numerical simulations makes the model-based optimization for the flow field architectures available. For instance, Yin et al. proposed a 3-D model of a vanadium redox flow battery (VRFB) with the IFF to optimize both the stack and the IFF designs, which focused on the parametric optimization rather than the structural optimization (Yin et al. 2014). Yaji et al. proposed a topology optimization for enabling a freeform flow field design in a VRFB (Yaji et al. 2018). However, the optimized flow field architecture was hardly practical due to the crooked channels. One practical approach is to combine several conventional flow channels to generate new flow fields. In this context, the present study aims to propose an optimization framework for a flow field that heterogeneously combines the interdigitated and serpentine flow channels, termed as interdigitated-serpentine flow field (ISFF) in the present study, with the objective of enhancing the system energy efficiency (pump losses included) of a VRFB flow cell. The present study provides possibilities for flow channel combinations and practical heterogeneous flow field architectures. Moreover, the present study may also contribute to the simultaneous optimization of the flow field and the electrode architecture (such as fiber diameter, porosity, and thickness of a porous electrode) (Tsushima and Suzuki 2020).

The rest of the paper proceeds as follows. First, the details of the devised optimization framework along with the hydraulic and the electrochemical models are presented in Section 2. The developed models are validated against experimental results, details of which are also presented in Section 2. Then, the comparisons among the performance of the cells with the ISFF, the IFF, and the SFF in terms of the resulting system energy efficiency are presented in Section 3. The comparisons are conducted in the cells with the active area corresponding to 25 cm^2 and 100 cm^2, respectively, for illustrating the differences in the small and large cells. Last, Section 4 concludes the paper.

2. Data and methods

2.1. Optimization framework

Generally, two distinct flow field units are identified for the IFF and the SFF, respectively, as shown in Figure 1. To be specific, an IFF unit consists of two disconnected flow passages and an SFF unit consists of two parallel flow passages and one corner channel connecting the two flow passages. One additional corner channel, which can be connected to the inlet or the outlet of the flow cell or other units, is also incorporated in the SFF unit. Then, an IFF section consisting one or several IFF units is formed by increasing the diversion of the flow channels that are connected by two guiding channels and an SFF section connects units by the corner channels (Figure 1). The whole domain of the flow field is shaped by randomly combining the IFF and the SFF sections in which the numbers of units are also randomly generated (e.g., Figure 1). In this sense, a great deal of potential flow field domains that consist of practical interdigitated and serpentine flow channels are generated.
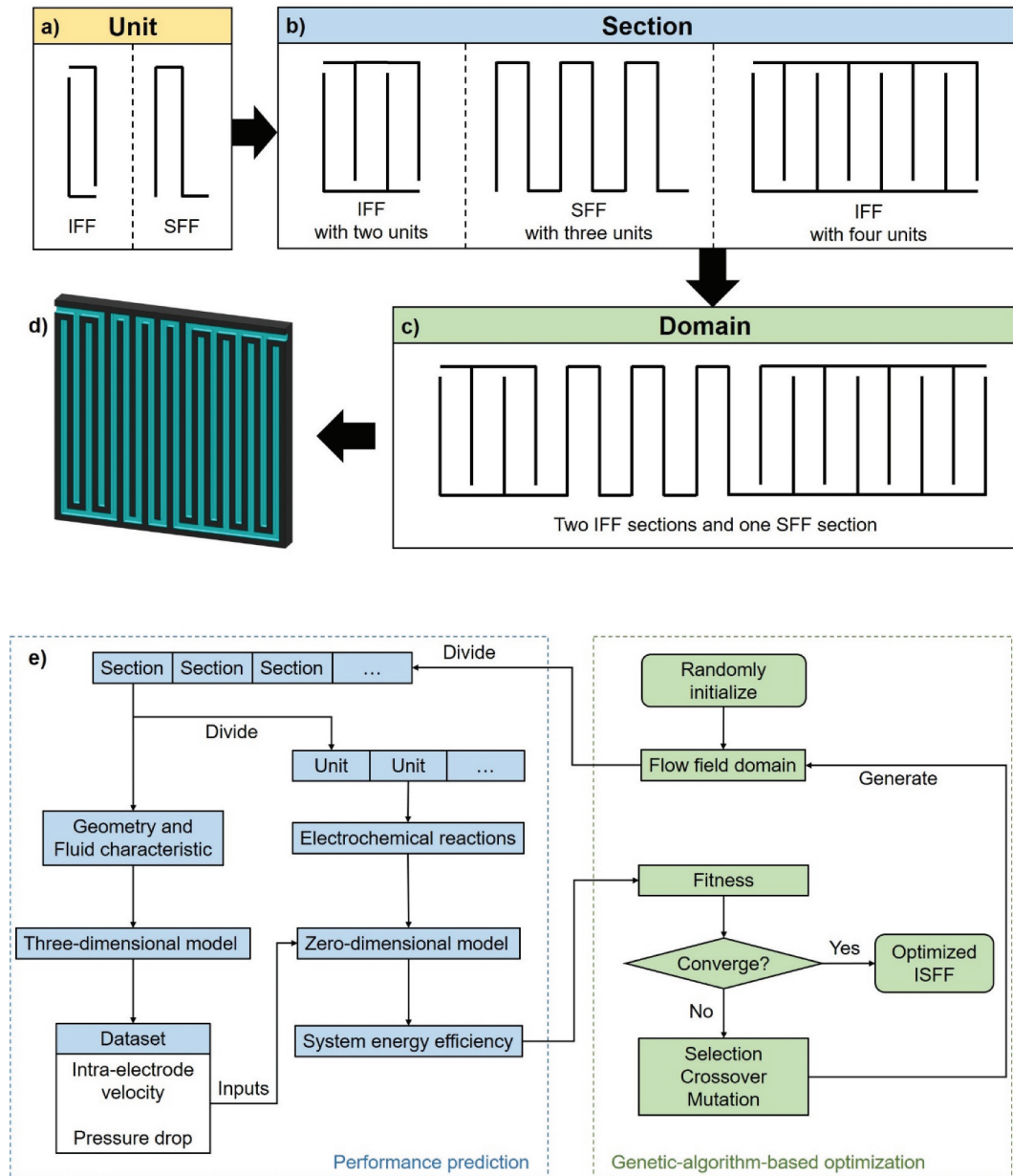
Figure 1. Illustrations of interdigitated and serpentine (a) unit and (b) section. (c)(d) Flow field domain with different combinations of interdigitated and serpentine sections. Note that the figures are not plotted to scale. (e) Illustration of the optimization framework. IFF denotes interdigitated flow field; SFF denotes serpentine flow field; and ISFF denotes interdigitated-serpentine flow field.

The present study proposes to make a trade-off between the accuracy of the prediction and the computational time by discretizing the flow domain into several flow sections and units. Simulation results illustrate that the IFF or the SFF sections are affected slightly by adjacent sections and the resulting intra-electrode flow. Rather, the corresponding pressure distribution is largely determined by the number of the IFF or the SFF units in one section. Thus, it is assumed that sections are independent of each other and a prepared dataset with the simulated hydrodynamic results for the representative sections for simplifying calculations. The dimensional effects caused by the flow field are simplified to two key performance results including the intra-electrode velocity and the pressure drop in one section, which are generated for each section. The two sets of the performance results are obtained by using

a three-dimensional fluid dynamic model and a dataset of the representative sections with varying numbers of the SFF or the IFF units is prepared for a quick prediction of a flow field domain. The steady-state, three-dimensional fluid dynamic model consisting of the Navier–Stokes equation for describing the free flow of fluids in the flow channels and the Brinkman equation for describing the flow within porous media is used to calculate the intra-electrode velocity and pressure distribution based on the steady flow assumption. Details of the three-dimensional model can be found in Section 2.2. The inlet flow condition of each section keeps the same value equaling the volumetric flow rate at the cell's inlet (Barton and Brushett 2019). The transient electrochemical reaction is then simulated for each unit to calculate the system energy efficiency by setting the averaged intra-electrode velocity in each unit as the input

in the zero-dimensional model, which includes the mass conservation, charge conservation, and energy conservation equations along with the Butler-Volmer equation describing the electrochemical behavior of the reactants. Besides, another essential input of the zero-dimensional model, i.e., the concentration of the reactants in each unit, is estimated by assuming that the concentration of the reactants is consumed equally in each unit no matter whether the unit takes the interdigitated or the serpentine form. With the above inputs, the system energy efficiency (pump losses excluded) of each unit is estimated accordingly and then the system energy efficiency of the whole domain is estimated by averaging the obtained efficiencies for all the units. The system energy efficiency is finally estimated by considering the averaged energy efficiency together with the summed pressure drops of all the units. Considering the large amount of the potential combinations of the SFF and the IFF units, the optimization for maximizing the system energy efficiency proceeds with the genetic algorithm (details can be found in Section 2.4). The above steps are illustrated as a flow chart in Figure 1. The accuracy of the proposed method for predicting the system energy efficiencies (pump losses included) of the flow cell is validated against the experimental results (Section 2.5).

To summarize, the proposed optimization framework for the ISFF is illustrated in Figure 1, with the following steps: (i) flow field generation, (ii) hydrodynamic performance prediction via the three-dimensional fluid dynamic model and the prepared dataset for the representative SFF and IFF sections, (iii) system energy efficiency prediction via the zero-dimensional electrochemical reaction model, and (iv) optimization via the genetic algorithm.

2.2. Three-dimensional fluid dynamic model

The governing equations such as the Navier–Stokes equation for describing the electrolyte flow in the flow channels and the Brinkman equation for describing the intra-electrode flow are solved by using the COMSOL Multiphysics software. The simulation process generally follows the reference (Houser et al. 2016). The geometric parameters of the flow channels and key parameters of the electrode, the positive and negative electrolytes, the electrochemistry, and the flow cell are provided in Table 1. The simulative charge and discharge curves under different operation conditions and pressure drops of the electrolyte flowing from the inlet to the outlet of the flow cell under the three different flow rates are compared with the experimentally measured results, which are presented in Section 2.5.

2.3. Zero-dimensional electrochemical reaction model

The electrochemical reaction model is built upon the previous work (Wang et al. 2018). As an essential input of the zero-dimensional electrochemical reaction model, the concentration of the reactants is consumed equally in each unit and estimated as below:

$$\frac{dc_{i,x+1}}{dt} = \frac{dc_{i,x}}{dt} \pm \frac{1}{k}\frac{I}{zF} \tag{1}$$

where $c_{i,x}$ denotes the concentration of the species i in the xth unit, k denotes the total number of the channels, SFF or IFF, in the whole domain, I denotes the applied current, z denotes the number of electron and F denotes Faraday's constant. The plus sign in the equation denotes the charging process, while the minus sign denotes the discharge process.

The system energy efficiency (pump losses included) is calculated for one complete charge and discharge cycle by using the following equation:

$$\eta_{\text{system}} = \frac{\int_{t=0}^{t=T}(I_{\text{discharge}}E_{\text{discharge}} - \Delta pQ)dt}{\int_{t=0}^{t=T}(I_{\text{charge}}E_{\text{charge}} + \Delta pQ)dt} \tag{2}$$

Where, η_{system} denotes the system energy efficiency (pump losses included), I denotes the applied charge or discharge current, E denotes the applied charge or discharge voltage, Δp denotes the pressure drop of the electrolyte flowing from the inlet to the outlet of the flow cell, Q denotes the flow rate of the electrolyte, and T denotes the charge or discharge duration.

2.4. Genetic-algorithm-based optimization model

The genetic algorithm proceeds as follows: (i) The flow field configuration is coded to form a binary chromosome, and thus an individual, with number zero denoting an IFF unit and number one denoting an SFF unit. The length of the chromosome is determined by the number of the units that can be fitted into the domain with the given geometric parameters of the channels and ribs (see Table 1), for example, 15 genes (i.e., 15 units) in one chromosome for the investigated electrode area corresponding to 25 cm^2. The population is then formed with a group of individuals and initialized. (ii) The fitness of each individual is evaluated according to the predicted system energy efficiency (pump losses included) of the flow cell, and better individuals are selected via the tournament selection. (iii) The selected individuals then go through the crossover and mutation steps to form a new generation. In the present study, the genetic-algorithm-based optimization for the arrangement of the IFF and the SFF units is conducted with the population size being set as 30 in the 5 × 5 cm^2 flow cell and set as 120 in the 10 × 10 cm^2 flow battery, the crossover probability as 0.8 and the mutation rate as 0.1. The set of the parameters yield a stable convergence of the resulting system energy efficiency of the flow cell after 300 generations (see *Supplementary Material*).

2.5. Model validation

For validating the accuracy of the proposed model, the simulated pressure drops of the electrolyte from the inlet to the outlet of the flow cell by using the developed fluid dynamic model are validated against the experimentally measured pressure drop results under the electrolyte flow rates corresponding to 20, 40, and 60 mL/min, respectively. And the resulting charge and discharge curves predicted by using the electrochemical model are validated against the experimental results under the applied current densities corresponding to 40, 50,

Table 1. Parameters of electrode, electrolyte, flow field, electrochemistry, and flow cell.

Parameters	Value	Unit	Description	Source
F	96,485.3	C/mol	Faraday constant	
R	8.314	$J/(mol \cdot K)$	Gas constant	
Parameters of carbon paper				
ε	0.82	/	Porosity of carbon paper	Provided by manufacturer
κ	3×10^{-12}	m^2	Permeability of carbon paper	Provided by manufacturer
t	6×10^{-4}	m	Thickness of electrode	Three layers of compressed carbon paper
A	2.5×10^{-3}	m^2	Area of electrode	
Parameters of electrolyte				
c	1.6×10^3	mol/m^3	Initial concentration of vanadium electrolyte	
c_h	4×10^3	mol/m^3	Initial concentration of protons	
ρ	1.3×10^3	kg/m^3	Density of vanadium electrolyte	(Ma, Zhang, and Xing 2011)
v	4.928×10^{-3}	$Pa \cdot s$	Viscosity of vanadium electrolyte	(Ma, Zhang, and Xing 2011)
Parameters of flow channel				
l	5×10^{-2}	m	Length of channel	
w	1×10^{-3}	m	Width of channel	
H	1×10^{-3}	m	Height of channel	
r	1×10^{-3}	m	Rib width of channel	
Parameters of electrochemistry				
a	1×10^{-6}	m^{-1}	Specific area of carbon paper	Measured
E_{neg}^0	−0.255	V	Standard potential for negative reaction	(Knehr et al. 2012)
E_{pos}^0	1.004	V	Standard potential for positive reaction	(Knehr et al. 2012)
k_{neg}	7×10^{-8}	m/s	Reaction rate constant for negative reaction	(Knehr et al. 2012)
k_{pos}	2.5×10^{-8}	m/s	Reaction rate constant for positive reaction	(Knehr et al. 2012)
a_-	0.45	/	Cathodic transfer coefficient for negative reaction	(Knehr et al. 2012)
a_+	0.55	/	Cathodic transfer coefficient for positive reaction	(Knehr et al. 2012)
Parameters of flow cell				
V	3×10^{-5}	m^3	Volume of a tank	
R	4.2×10^{-2}	Ω	Resistance of a cell	Measured

and 60 mA/cm², respectively. The experimental setups are as follows. Three layers of carbon paper (SGL, Sigracet 38 AA, thickness of each layer corresponding to 280 μm) with the area corresponding to 25 cm² were compressed to 71% of the original thickness as the electrodes. The electrolytes containing the 1.6 M vanadium in the 4 M sulfuric acid were circulated by using the peristaltic pumps (Masterflex, L/S 07525–40) at the flow rate ranging from 20 to 60 mL/min according to the specific requirements. Two piezometers (TemTech PTFE)

were placed at the cell's inlet and outlet, respectively, to measure the pressure drop of the electrolyte flowing through the flow cell. The galvanostatic charge and discharge tests were performed with the upper and lower limits to the voltage being set as 1.6 V and 1.1 V, respectively, by using a Bio-logic® VSP electrochemical workstation. The electrolyte volumes in the positive and negative tanks are both set as 30 mL for maintaining the stable charge and discharge of the flow cell. To avoid side reactions and ensure the stability of the battery charge and discharge, the nitrogen was aerated to the negative tank and the experiments were conducted under a constant room temperature corresponding to 25°C.

As Figure 2 shows, charge and discharge curves and pressure drops of the electrolyte in the flow cells with the IFF and SFF are obtained by the simulative and experimental methods. Overall, the simulative charge and discharge curves show an agreement with the experimentally measured results (see Figure 2 and 2b), and the relative errors of the resulting system energy efficiencies compared to the measured results are less than 3%. The results obtained for the SFF and the IFF both show similar discrepancies. Specifically, larger discrepancies are observed in the discharge curves compared to the charge curves, which may be attributable to the crossover of the reactants, which was observed in the experiments but not considered in the current version of the zero-dimensional electrochemical reaction model. With respect to the pressure drop results as shown in Figure 2 and 2d, the high uncertainties in the measured results are generally due to the accuracy limitation of the pressure sensors (provided by Tem-Tech Lab, with the testing range corresponding to 0 to 50 psi and an accuracy of ±1% full scale). Nevertheless, the differences in the pressure drop results discussed in Section 3 are beyond the relative errors between the simulative and experimentally measured results.

3. Results

3.1. System efficiencies of small flow cells with IFF, SFF, and ISFF

The concentration overpotential, pump losses, and corresponding system energy efficiencies of the flow cells with the SFF, the IFF, and the optimized ISFF under the current densities corresponding to 40, 50, and 60 mA/cm², respectively, and the electrolyte flow rates corresponding to 20, 40, and 60 mL/min, respectively, are displayed in Figures 3 and 4. Note that all the results are obtained simulatively by using the experimentally validated models. The optimized arrangements for the IFF and SFF units are presented in Table 2. The results with respect to the overall system energy efficiency illustrate that the flow cells with the IFF perform better than the cells with the SFF at relatively high flow rates (e.g., 60 mL/min), which is partly due to the large flow velocities in the cell with the SFF. Compared with the SFF, the volumetric electrolyte flow is divided into the IFF units within each section. Thereby, sharp increments in the concentration overpotential as shown in Figure 4, 4b, and 4c and thereby reductions in the system energy efficiency of the cell are observed in the cell with the IFF. For example, the concentration overpotential is increased
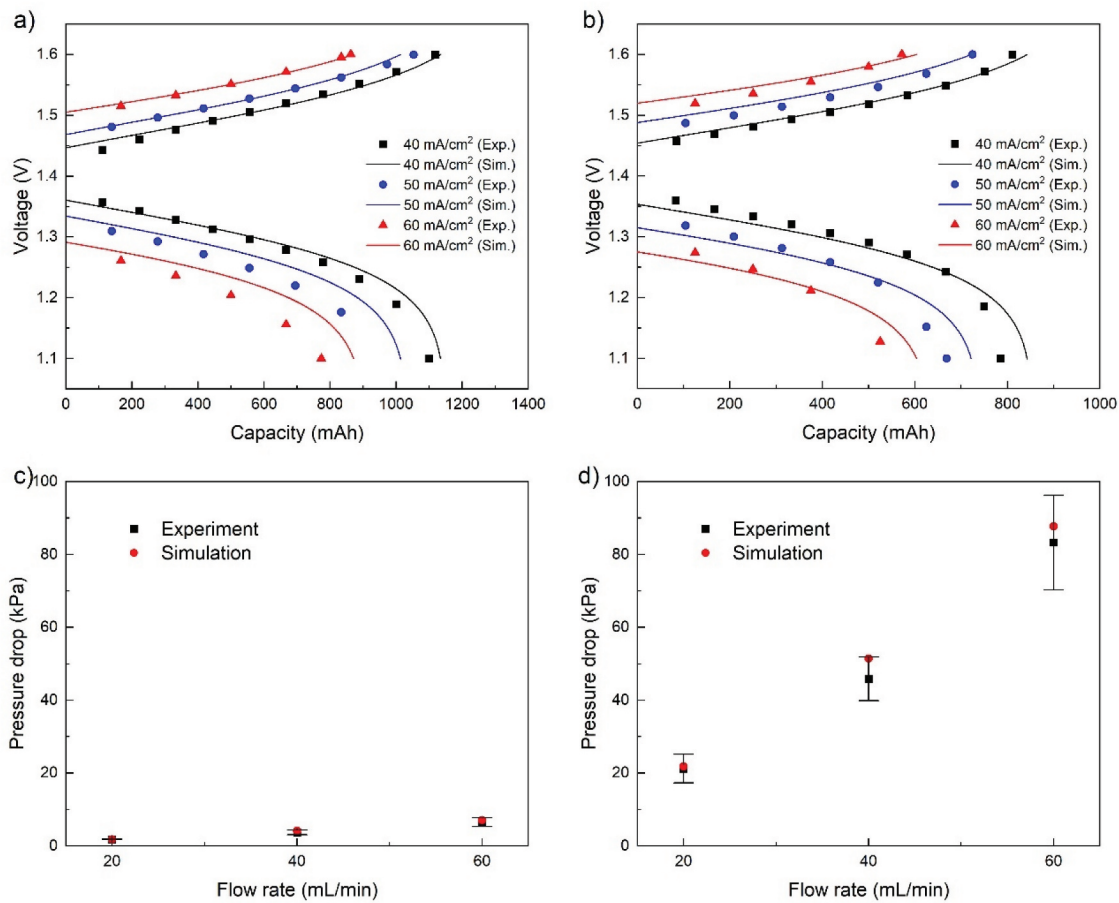
Figure 2. Comparisons between the experimental and simulative results: charge and discharge curves of the flow cells with (a) IFF and (b) SFF under the current density corresponding to 40, 50, and 60 mA/cm^2 and the electrolyte flow rate corresponding to 40 mL/min and 10 ml/min; pressure drops of the electrolyte flowing from the inlet to the outlet of the flow cell with (a) IFF and (b) SFF under the flow rate corresponding to 20, 40, and 60 mL/min.

from 43 mV to 81 mV at the state of charge corresponding to 20% and the system energy efficiency is increased from 72% to 84%, when the current density increases from 40 to 60 mA/cm^2 (flow rate corresponding to 40 mL/min). By contrast, the SFF leads to sharp reductions in the system energy efficiency of the cell at large flow rates owing to the significant increments in the pump losses. As shown in Figure 4, the pressure loss increases by 12 folds under the SFF when the flow rate increases from the 40 to 60 mL/min. And under the flow rate corresponding to 60 mL/min and the current density corresponding to 40 mA/cm^2, the pump losses account for approximately 14.4% of the charged energy in the cell with the SFF. The similar observations can also be found in the previous studies (Gundlapalli and Jayanti 2020b). By making a trade-off between the alleviated concentration overpotential and the reduced pump losses, the proposed ISFF adjusts the electrolyte flow velocities by combing the IFF and the SFF units. Under the investigated operation conditions, the optimized ISFF yields the best performance among the three flow fields, with the increments in the system energy efficiencies (pump losses included) ranging from 2% to 20% compared to the better ones between the IFF and the SFF cases under varying operation conditions.

As shown in Figures 3 and 4, the IFF outperforms the SFF particularly under large flow rates. Therefore, the optimized ISFFs under the flow rates corresponding to 60 mL/min take the form of the IFF expect for the condition when the applied

current density is set as 60 mA/cm^2. As the flow rate decreases or the current density increases, more SFF units are fitted into the optimized flow field to enhance the mass transfer capability of the reactor by increasing the intra-electrode velocity of the electrolyte. In this manner, the IFF units are divided into several sections with less IFF units, and thereby higher intra-electrode electrolyte velocities in each section. It should be noted that the above results are based upon the small flow cell with the electrode area corresponding to 25 cm^2 where the reactants are generally homogeneously distributed from the inlet to the outlet of the flow cell. Therefore, the optimized arrangements for the IFF and the SFF units are also homogeneously distributed. The implication of the proposed ISFF for the large flow cell will be addressed in the next subsection.

3.2. System energy efficiencies of large flow cells with IFF, SFF, and ISFF

The heterogeneous mass transfer requirements due to the concentration distribution can be amplified by the size of the flow cell. Thus, the study on the large flow cell with an active area corresponding to 100 cm^2 is investigated and the system energy efficiency and velocity distribution results of the flow cell with the ISFF are compared with those of the flow cells with the IFF and the SFF as shown in Figure 5. The optimized
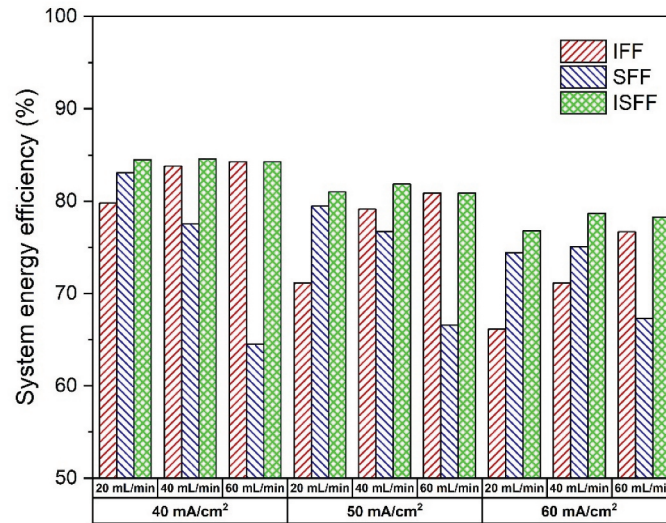
Figure 3. System energy efficiencies of the flow cells with the IFF, the SFF, and the ISFF at the current density corresponding to 40, 50, and 60 mA/cm², respectively, and the electrolyte flow rate corresponding to 20, 40, and 60 mL/min, respectively. IFF denotes interdigitated flow field; SFF denotes serpentine flow field; and ISFF denotes interdigitated-serpentine flow field. Results are obtained via simulations.

Figure 4. Concentration overpotential of the flow cells with the IFF, the SFF, and the optimized ISFF, under the current density corresponding to (a) 40, (b) 50, and (c) 60 mA/cm² and the electrolyte flow rate corresponding to 40 mL/min. and (d) pump losses when the electrolyte flows from the inlet to the outlet of flow cells under the electrolyte flow rate corresponding to 20, 40, and 60 mL/min, respectively. IFF denotes interdigitated flow field; SFF denotes serpentine flow field; and ISFF denotes interdigitated-serpentine flow field. Results are obtained via simulations.
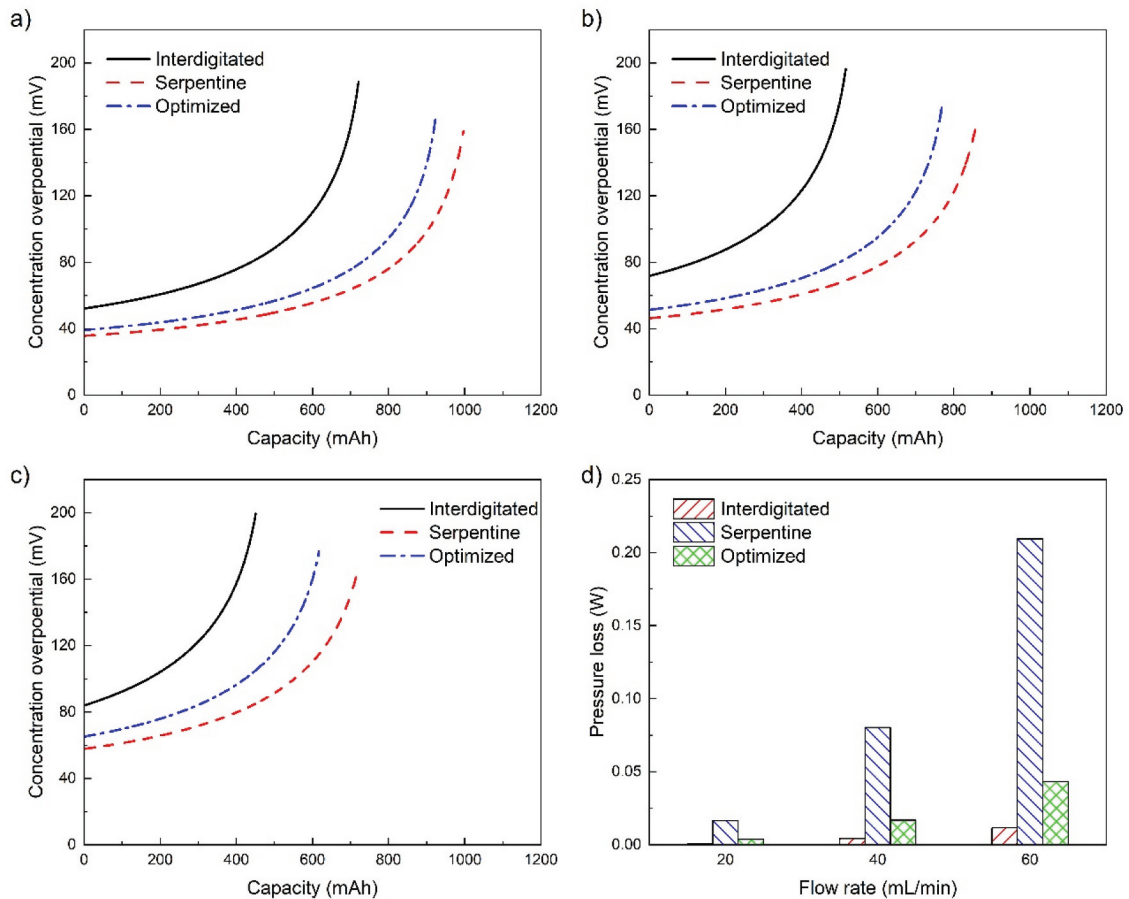
Table 2. Optimized interdigitated-serpentine flow field configuration under various operating conditions.

Current density mA/cm²	Flow rate mL/min	Optimized interdigitated-serpentine flow field configuration (with 12 units) Where "I" denotes interdigitated unit and "S" denotes serpentine unit											
40	20	I	I	I	I	S	S	S	S	I	I	I	I
	40	I	I	I	I	I	S	I	I	I	I	I	I
	60	I	I	I	I	I	I	I	I	I	I	I	I
50	20	I	I	S	S	S	I	I	S	S	S	I	I
	40	I	I	I	I	I	S	I	I	I	I	I	I
	60	I	I	I	I	I	I	I	I	I	I	I	I
60	20	I	I	S	S	S	I	I	S	S	S	I	I
	40	I	I	I	I	I	I	S	I	I	I	I	I
	60	I	I	I	I	I	S	I	I	I	I	I	I

configurations of the ISFF under different operating conditions are presented in Table 3. Although the system energy efficiencies decrease in the large flow cells compared to those predicted in the small flow cells (Figure 3), the trends of the efficiencies varying with the applied electrolyte flow rate and the current density are consistent with the observations in the small flow cells. In addition, less IFF units are generated in each IFF section and more SFF units are observed in the optimized ISFFs when the flow rate decreases or the current density increases (Table 3). Under the investigated operation conditions, the ISFF yields the best performance among the three flow fields with the increments in the system energy efficiencies ranging from 1.7% to 20% compared to the better ones between the SFF and the IFF conditions. The consistent performance enhancement indicates that the proposed ISFF architecture along with the optimization framework is effective for both large and small flow cells.

Nevertheless, the heterogeneous distribution of the reactants in the large flow cells yields variations in the optimized arrangements of the SFF and the IFF units in the optimized ISFF (Table 2) compared to those obtained in the small flow cells (Table 3). As shown in Table 3, the optimized IFF units are heterogeneously distributed in the large flow cells with less IFF units in one IFF section close to the outlet than those close to the inlet of the cells. Such arrangement further enhances the mass transfer close to the outlet as the reactants are consumed gradually from the inlet to the outlet of the cells.

3.3. Extension of flow field units

The ISFF proposed in the present study is generated based on the interdigitated and the serpentine units, the promotion in the system energy efficiency of which is achieved by synthesizing the advantages of these two distinct units. It is expected that the integration of more unit types further improves the performance of the flow cell. As an extension of the devised ISFF architecture, the half-serpentine (HSFF, as shown in Figure 6) is also considered as one potential unit for the flow field. The half-serpentine flow field consists of two parallel flow passages and one connecting passage located in the middle of the pair of the parallel passages as shown in Figure 6. The half-serpentine flow field combines with the interdigitated or the serpentine flow field by two diagonal channels. The proposed optimization is thus conducted for the three units, i.e., IFF, SFF, and HSFF, and the corresponding results are provided in Figure 6 and Table 4. Results show that the addition of the HSFF unit
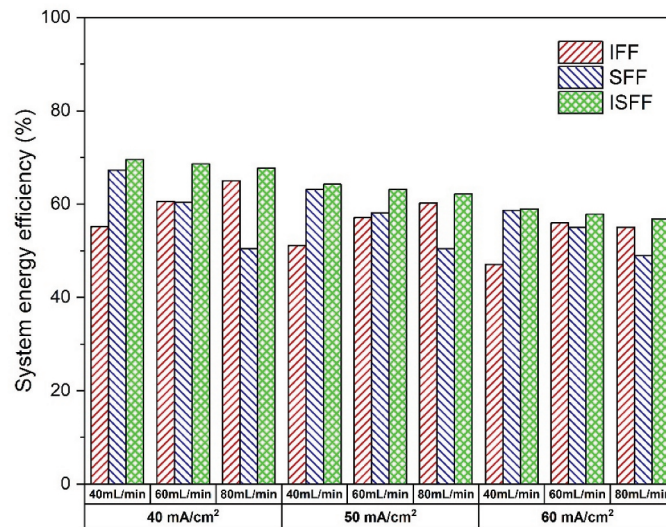

Figure 5. System energy efficiencies of the 100 cm² area flow cells with the IFF, the SFF, and the ISFF at the current density corresponding to 40, 50, and 60 mA/cm², respectively, and the electrolyte flow rate corresponding to 40, 60, and 80 mL/min, respectively. IFF denotes interdigitated flow field; SFF denotes serpentine flow field; and ISFF denotes interdigitated-serpentine flow field. Results are obtained via simulations.

Table 3. Optimized interdigitated-serpentine flow field configuration under various operating conditions.

Current density mA/cm^2	Flow rate mL/min	Optimized interdigitated-serpentine flow field configuration (with 25 units) Where "I" denotes interdigitated unit and "S" denotes serpentine unit
40	40	I I I I S I I I I S I I I S I I I I S I I I I S I I I
	60	I I I I I I I I I S I I I I I I I I S I I I I I I I I
	80	I I I I I I I I I I I S I I I I I I I I I I I I I I
50	40	I I I S I I I I S I I I S I I I S S I I I I S S I I I
	60	I I I I I I I I S I I I I I S I I I I I I S I I I I
	80	I I I I I I I I I S I I I I I I I I S I I I I I I I
60	40	I I S S I I S S I I S I I S S I I S S I I S S I I
	60	I I I I I S I I I I I I S I I I I I I S I I I S I I I
	80	I I I I I I I S I I I I I I I S I I I I I I S I I I I

further increases the system energy efficiencies slightly. The HSFF unit compared to the SFF unit moves the corner channels to the middle of the flow passages, thereby reducing the flow resistance near the connecting passage and thereby the overall flow resistance. In this manner, the pressure drop of the electrolyte and the intra-electrode velocity are simultaneously reduced. Thus, under the low current density conditions such as 40 and 50 mA/cm^2, the HSFF unit performs better than the SFF unit. It should be noted that although the additional system energy efficiency promotions are limited, this example shows the probabilities to further improve the optimization by increasing the types of the units. For example, a number of

novel flow fields have been proposed in previous studies, which are sources for the potential basic flow field units to be incorporated in the future.

3.4. Future work

Although the proposed optimization framework for the combined interdigitated and serpentine flow channels effectively improves the system energy efficiencies of the small and large flow cells, the accuracy of the involved models is expected to be improved, and the work is also expected to incorporate novel flow field units in the future. First, some assumptions and
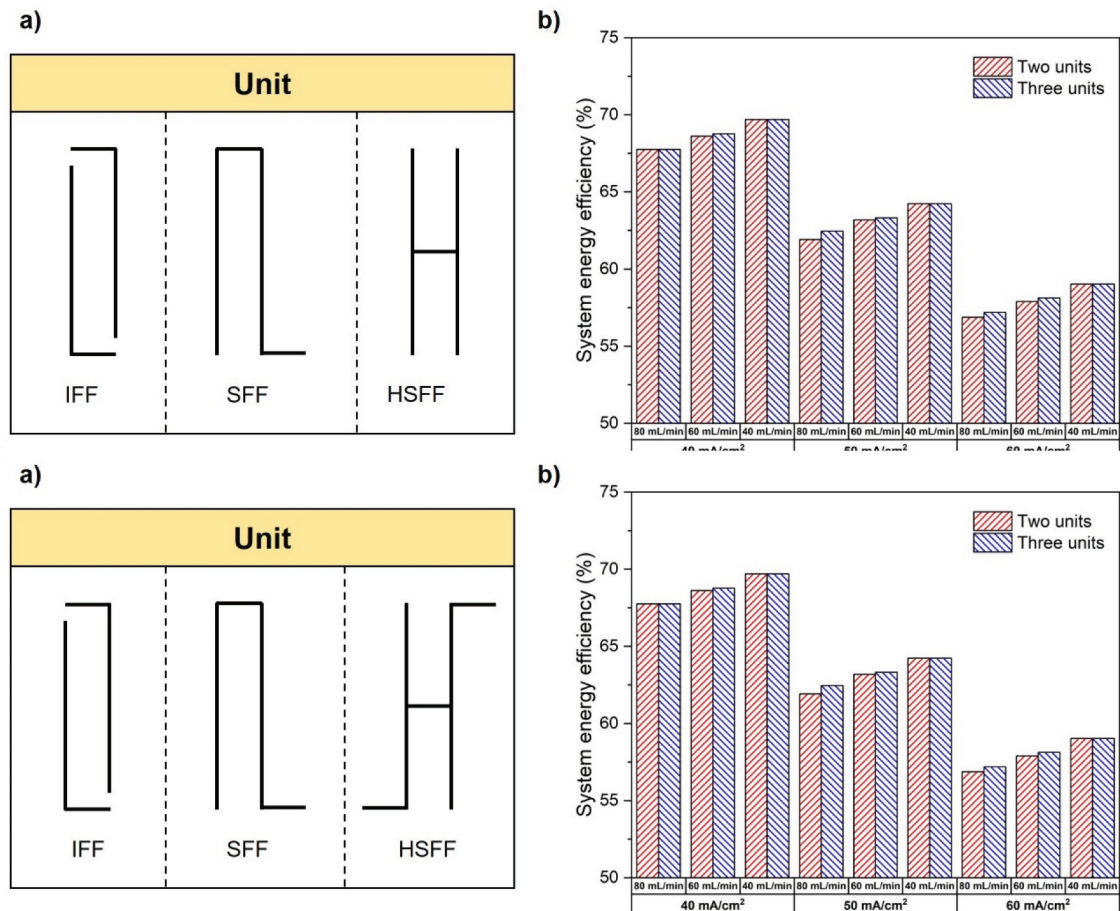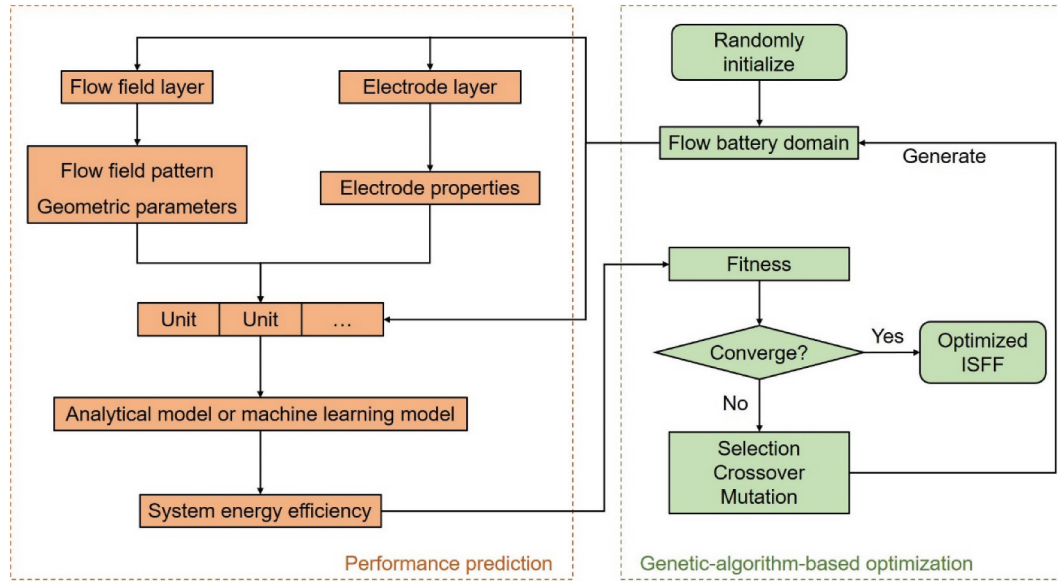

Figure 6. (a) Diagram of the interdigitated flow field (IFF) unit, the serpentine flow field (SFF) unit and the half-serpentine flow field (HSFF) unit. (b) Comparisons of system energy efficiencies between optimized cells with two types (IFF and SFF) and three types of units (IFF, SFF, and HSFF).

Table 4. Optimized interdigitated-serpentine flow field configuration with three units under various operating conditions.

Current density mA/cm²	Flow rate mL/min	Optimized interdigitated-serpentine flow field configuration (with 25 units) Where "I" denotes interdigitated unit, "S" denotes serpentine unit and "H" denotes half-serpentine unit
40	40	I I I I I I I H H I I I I I I H I I I I I I H I I I I I I
	60	I I I I I I I H H I I I I I I I I I I H I I I I I I I I
	80	I I I I I I I I I I I I H I I I I I I I I I I I I I
50	40	I I I H I I I H I I I I I H I I I H I I I H I I I I
	60	I I I I I H I I I I I I H I I I I H I I I I I H I I I
	80	I I I I I I I I I H I I I I I I I H I I I I I I I I
60	40	I I S S I I S S I I S I I S S I I S S I I S S I I
	60	I I I I I S I I I I I S I I I I I S I I I S I I I
	80	I I I I I I I S I I I I I I S I I I I I S I I I I

Figure 7. Extended optimization framework considering flow field pattern, geometric parameters of flow channels, and electrode properties based on the genetic algorithm. ISFF denotes interdigitated-serpentine flow field.

simplifications are made in the present study to make a trade-off between the accuracy and the computational time consumption. This contradiction is expected to be mitigated by advanced algorithms such as machine learning methods, e.g. (Bao et al. 2020), combined with a prepared dataset obtained via a 3-D multi-physics coupling model. Second, more practical flow field units should be incorporated in the optimization to extend the potential combinations of the flow channels (see Section 3.3). Besides, recognizing that the proposed model-based optimization method is supposed to improve the system energy efficiency by combining practical flow channels in a feasible way, there will be advantages with respect to the cost compared to other novel flow fields such as spiral, bio-inspired, and trapezoid flow fields. Nevertheless, detailed cost and durability analysis of the proposed novel flow field in real applications should be conducted in future work. Last but not least, the recent advances in the electrode materials call for a simultaneous optimization for the flow field and the electrode architecture, which should be one essential extension of the current work. The geometric parameters of the flow channels and the properties of the electrode can be optimized simultaneously with the type of the flow channels in future work according to an extended version of the optimization framework (as shown in Figure 7). Considering the potential large amount of combinations of the geometric parameters, the electrode material, and the flow channels, the battery performance is expected to be fast predicted by using analytical models or via the machine learning method for accelerating the computational speed.

4. Conclusions

The present study proposed a model-based optimization method for the flow field in RFBs that combines the interdigitated and the serpentine channels heterogeneously to generate the ISFF for enhancing the mass transfer at low expenses of the pump losses, matching the concentration gradient of the reactants in the in-plane direction of the electrode, and then promoting the system energy efficiency (pump losses included) during charge and discharge cycles. The results proved possibilities of combining different flow field units that the increments of the system energy efficiency ranging from 2% to 20% were performed in the flow cells with the ISFF compared to IFF and SFF. Moreover, the ISFF implemented in the large-scale flow cell also showed superiorities compared to the conventional IFF and SFF and the optimized distribution of the flow units are heterogeneously to match the heterogeneous distribution of the reactants in

the in-plane direction of the electrode. Although the proposed optimization framework effectively enhanced the system energy efficiency of the flow cell, limitations of the models remained owing to the assumptions made to reduce the computational time, which should be improved in future work. Great prospects of the proposed optimization method can be expected in the field of the flow field design for RFBs if a number of practical flow field units are added into the dataset.

Disclosure statement

Funding

References

Akuzum, B., Y. C. Alparslan, N. C. Robinson, E. Agar, and E. C. Kumbur. 2019. Obstructed flow field designs for improved performance in vanadium redox flow batteries. *Journal of Applied Electrochemistry* 49 (6):551–61. doi:10.1007/s10800-019-01306-1.

Bao, J., V. Murugesan, C. J. Kamp, Y. Y. Shao, L. T. Yan, and W. Wang. 2020. Machine learning coupled multi-scale modeling for redox flow batteries. *Advanced Theory and Simulations* 3 (2): 1900167. doi:10.1002/adts.201900167.

Barton, J. L., and F. R. Brushett. 2019. A one-dimensional stack model for redox flow battery analysis and operation. *Batteries-Basel* 5 (1): 25. doi:10.3390/batteries5010025.

Darling, R. M., and P. Badrinarayanan. 2011. Oxygen transport in polymer-electrolyte fuel cells with interdigitated air channels in porous bipolar plates. *Journal of the Electrochemical Society* 158 (1):B54–B60. doi:10.1149/1.3509159.

Darling, R. M., and M. L. Perry. 2014. The influence of electrode and channel configurations on flow battery performance. *Journal of the Electrochemical Society* 161 (9):A1381–A7. doi:10.1149/2.0941409jes.

Gundlapalli, R., and S. Jayanti. 2019. Effect of channel dimensions of serpentine flow fields on the performance of a vanadium redox flow battery. *Journal of Energy Storage* 23:148–58. doi:10.1016/j.est.2019.03.014.

Gundlapalli, R., and S. Jayanti. 2020a. Effect of electrolyte convection velocity in the electrode on the performance of vanadium redox flow battery cells with serpentine flow fields. *Journal of Energy Storage* 30:101516. doi:10.1016/j.est.2020.101516.

Gundlapalli, R., and S. Jayanti. 2020b. Performance characteristics of several variants of interdigitated flow fields for flow battery applications. *Journal of Power Sources* 467:228225 doi:10.1016/j.jpowsour.2020.228225.

Guo, N. N., M. C. Leu, and U. O. Koylu. 2014. Bio-inspired flow field designs for polymer electrolyte membrane fuel cells. *International Journal of Hydrogen Energy* 39 (36):21185–95. doi:10.1016/j.ijhydene.2014.10.069.

Gurieff, N., V. Timchenko, and C. Menictas. 2018. Variable porous electrode compression for redox flow battery systems. *Batteries-Basel* 4 (4). doi:10.3390/batteries4040053.

Houser, J., J. Clement, A. Pezeshki, and M. M. Mench. 2016. Influence of architecture and material properties on vanadium redox flow battery performance. *Journal of Power Sources* 302:369–77. doi:10.1016/j.jpowsour.2015.09.095.

Houser, J., A. Pezeshki, J. T. Clement, D. Aaron, and M. M. Mench. 2017. Architecture for improved mass transport and system performance in redox flow batteries. *Journal of Power Sources* 351:96–105. doi:10.1016/j.jpowsour.2017.03.083.

Huang, Z. B., A. L. Mu, L. X. Wu, H. Wang, and Y. J. Zhang. 2021. Electrolyte flow optimization and performance metrics analysis of vanadium redox flow battery for large-scale stationary energy storage. *International Journal of Hydrogen Energy* 46 (63):31952–62. doi:10.1016/j.ijhydene.2021.06.220.

Huskinson, B., M. P. Marshak, C. Suh, S. Er, M. R. Gerhardt, C. J. Galvin, X. D. Chen, A. Aspuru-Guzik, R. G. Gordon, and M. J. Aziz. 2014. A metal-free organic-inorganic aqueous flow battery. *Nature* 505 (7482):195±. doi:10.1038/nature12909.

Ke, X. Y., J. I. D. Alexander, J. M. Prahl, and R. F. Savinell. 2014. Flow distribution and maximum current density studies in redox flow batteries with a single passage of the serpentine flow channel. *Journal of Power Sources* 270:646–57. doi:10.1016/j.jpowsour.2014.07.155.

Ke, X. Y., J. I. D. Alexander, J. M. Prahl, and R. F. Savinell. 2015. A simple analytical model of coupled single flow channel over porous electrode in vanadium redox flow battery with serpentine flow channel. *Journal of Power Sources* 288:308–13. doi:10.1016/j.jpowsour.2015.04.138.

Ke, X. Y., J. M. Prahl, J. I. D. Alexander, and R. F. Savinell. 2018. Redox flow batteries with serpentine flow fields: Distributions of electrolyte flow reactant penetration into the porous carbon electrodes and effects on performance. *Journal of Power Sources* 384:295–302. doi:10.1016/j.jpowsour.2018.03.001.

Knehr, K. W., E. Agar, C. R. Dennison, A. R. Kalidindi, and E. C. Kumbur. 2012. A transient vanadium flow battery model incorporating vanadium crossover and water transport through the membrane. *Journal of the Electrochemical Society* 159 (9):A1446–A59. doi:10.1149/2.017209jes.

Kumar, S., and S. Jayanti. 2016. Effect of flow field on the performance of an all-vanadium redox flow battery. *Journal of Power Sources* 307:782–87. doi:10.1016/j.jpowsour.2016.01.048.

Kumar, S., and S. Jayanti. 2017. Effect of electrode intrusion on pressure drop and electrochemical performance of an all-vanadium redox flow battery. *Journal of Power Sources* 360:548–58. doi:10.1016/j.jpowsour.2017.06.045.

Latha, T. J., and S. Jayanti. 2014. Hydrodynamic analysis of flow fields for redox flow battery applications. *Journal of Applied Electrochemistry* 44 (9):995–1006. doi:10.1007/s10800-014-0720-0.

Lee, J., J. Kim, and H. Park. 2019. Numerical simulation of the power-based efficiency in vanadium redox flow battery with different serpentine channel size. *International Journal of Hydrogen Energy* 44 (56):29483–92. doi:10.1016/j.ijhydene.2019.05.013.

Ma, X.K., H.M. Zhang and F. Xing. 2011. A three-dimensional model for negative half cell of the vanadium redox flow battery. *Electrochimica Acta* 58:238–46. doi:10.1016/j.electacta.2011.09.042.

Maurya, S., P. T. Nguyen, Y. S. Kim, Q. J. Kang, and R. Mukundan. 2018. Effect of flow field geometry on operating current density, capacity and performance of vanadium redox flow battery. *Journal of Power Sources* 404:20–27. doi:10.1016/j.jpowsour.2018.09.093.

Noack, J., L. Wietschel, N. Roznyatovskaya, K. Pinkwart, and J. Tubke. 2016. Techno-Economic modeling and analysis of redox flow battery systems. *Energies* 9 (8). doi: 10.3390/en9080627.

Pan, F., and Q. Wang. 2015. Redox species of redox flow batteries: A Review. *Molecules* 20 (11):20499–517. doi:10.3390/molecules201119711.

Park, J., and X. G. Li. 2011. An analytical analysis on the cross flow in a PEM fuel cell with serpentine flow channel. *International Journal of Energy Research* 35 (7):583–93. doi:10.1002/er.1712.

Shigematsu, T. 2019. The development and demonstration status of practical flow battery systems. *Current Opinion in Electrochemistry* 18:55–60. doi:10.1016/j.coelec.2019.10.001.

Skyllas-Kazacos, M., M. H. Chakrabarti, S. A. Hajimolana, F. S. Mjalli, and M. Saleem. 2011. Progress in flow battery research and development. *Journal of the Electrochemical Society* 158 (8):R55–R79. doi:10.1149/1.3599565.

Su, A., F. B. Weng, C. Y. Hsu, and Y. M. Chen. 2006. Studies on flooding in PEM fuel cell cathode channels. *International Journal of Hydrogen Energy* 31 (8):1031–39. doi:10.1016/j.ijhydene.2005.12.019.

Sun, J., M. L. Zheng, Y. S. Luo, and Z. T. Yu. 2019. Three-Dimensional detached serpentine flow field design for redox flow batteries. *Journal of Power Sources* 428:136–45. doi:10.1016/j.jpowsour.2019.04.106.

Tsushima, S., and T. Suzuki. 2020. Modeling and simulation of vanadium redox flow battery with interdigitated flow field for optimizing electrode architecture. *Journal of the Electrochemical Society* 167 (2). doi:10.1149/1945-7111/ab6dd0.

Wang, T., J. H. Fu, M. L. Zheng, and Z. T. Yu. 2018. Dynamic control strategy for the electrolyte flow rate of vanadium redox flow batteries. *Applied Energy* 227:613–23. doi:10.1016/j.apenergy.2017.07.065.

Wang, W., Q. T. Luo, B. Li, X. L. Wei, L. Y. Li, and Z. G. Yang. 2013. Recent progress in redox flow battery research and development. *Advanced Functional Materials* 23 (8):970–86. doi:10.1002/adfm.201200694.

Weber, A. Z., M. M. Mench, J. P. Meyers, P. N. Ross, J. T. Gostick, and Q. H. Liu. 2011. Redox flow batteries: A review. *Journal of Applied Electrochemistry* 41 (10):1137–64. doi:10.1007/s10800-011-0348-2.

Xu, Q., T. S. Zhao, and C. Zhang. 2014. Performance of a vanadium redox flow battery with and without flow fields. *Electrochimica Acta* 142:61–67. doi:10.1016/j.electacta.2014.07.059.

Yaji, K., S. Yamasaki, S. Tsushima, T. Suzuki, and K. Fujita. 2018. Topology optimization for the design of flow fields in a redox flow battery. *Structural and Multidisciplinary Optimization* 57 (2):535–46. doi:10.1007/s00158-017-1763-8.

Yin, C., Y. Gao, S. Y. Guo, and H. Tang. 2014. A coupled three dimensional model of vanadium redox flow battery for flow field designs. *Energy* 74:886–95. doi:10.1016/j.energy.2014.07.066.

Yoon, S. J., S. Kim, and D. K. Kim. 2019. Optimization of local porosity in the electrode as an advanced channel for all-vanadium redox flow battery. *Energy* 172:26–35. doi:10.1016/j.energy.2019.01.101.

Yue, M., Q. Zheng, F. Xing, H. M. Zhang, X. F. Li, and X. K. Ma. 2018. Flow field design and optimization of high power density vanadium flow batteries: A novel trapezoid flow battery. *AIChE Journal* 64 (2):782–95. doi:10.1002/aic.15959.

Zhang, S., X. Li, and D. D. Chu. 2016. An organic electroactive material for flow batteries. *Electrochimica Acta* 190:737–43. doi:10.1016/j.electacta.2015.12.139.

Zhang, X. Y., X. Zhang, H. Taira, and H. T. Liu. 2018. Error of Darcy's law for serpentine flow fields: An analytical approach. *International Journal of Hydrogen Energy* 43 (13):6686–95. doi:10.1016/j.ijhydene.2018.02.070.

Zheng, Q., F. Xing, X. F. Li, G. L. Ning, and H. M. Zhang. 2016. Flow field design and optimization based on, the mass transport polarization regulation in a flow-through type vanadium flow battery. *Journal of Power Sources* 324:402–11. doi:10.1016/j.jpowsour.2016.05.110.